remote sensing

MDPI

Technical Note

Optical Properties and Possible Origins of Atmospheric Aerosols over LHAASO in the Eastern Margin of the Tibetan Plateau

Junji Xia [1], Fengrong Zhu [1,2,*], Xingbing Zhao [3], Jing Liu [1], Hu Liu [1], Guotao Yuan[1], Qinning Sun [1], Lei Xie [1], Min Jin [1], Long Chen [1], Yang Wang [1], Yu Liu [1] and Tengfei Song [4]

[1] The School of Physical Science and Technology, Southwest Jiaotong University, Chengdu 611756, China; xiajunji@my.swjtu.edu.cn (J.X.)
[2] Science School, Tibet University, Tibet 850000, China
[3] Institute of Plateau Meteorology, CMA, No.20 Guanghuacun Street, Chengdu 610072, China
[4] Yunnan Observatories, Chinese Academy of Sciences, No. 396, Yangfangwang, Kunming 650011, China
* Correspondence: zhufr@swjtu.edu.cn

Abstract: The accuracy of cosmic ray observations by the Large High Altitude Air Shower Observatory Wide Field-of-View Cherenkov/Fluorescence Telescope Array (LHAASO-WFCTA) is influenced by variations in aerosols in the atmosphere. The solar photometer (CE318-T) is extensively utilized within the Aerosol Robotic Network as a highly precise and reliable instrument for aerosol measurements. With this CE318-T 23, 254 sets of valid data samples over 394 days from October 2020 to October 2022 at the LHAASO site were obtained. Data analysis revealed that the baseline Aerosol Optical Depth (AOD) and Ångström Exponent (AE) at 440–870 nm ($AE_{440–870nm}$) of the aerosols were calculated to be 0.03 and 1.07, respectively, suggesting that the LHAASO site is among the most pristine regions on Earth. The seasonality of the mean AOD is in the order of spring > summer > autumn = winter. The monthly average maximum of AOD_{440nm} occurred in April (0.11 ± 0.05) and the minimum was in December (0.03 ± 0.01). The monthly average of $AE_{440–870nm}$ exhibited slight variations. The seasonal characterization of aerosol types indicated that background aerosol predominated in autumn and winter, which is the optimal period for the absolute calibration of the WFCTA. Additionally, the diurnal daytime variations of AOD and AE across the four seasons are presented. Our analysis also indicates that the potential origins of aerosol over the LHAASO in four seasons were different and the atmospheric aerosols with higher AOD probably originate mainly from Northern Myanmar and Northeast India regions. These results are presented for the first time, providing a detailed analysis of aerosol seasonality and origins, which have not been thoroughly documented before in this region, also enriching the valuable materials on aerosol observation in the Hengduan Mountains and Tibetan Plateau.

Keywords: aerosol optical depth (AOD); sun photometer; aerosol optical properties; aerosol potential origin

check for updates

Citation: Xia, J.; Zhu, F.; Zhao, X.; Liu, J.; Liu, H.; Yuan, G.; Sun, Q.; Xie, L.; Jin, M.; Chen, L.; et al. Optical Properties and Possible Origins of Atmospheric Aerosols over LHAASO in the Eastern Margin of the Tibetan Plateau. *Remote Sens.* **2024**, *16*, 1695. https://doi.org/10.3390/rs16101695

Academic Editor: Manuel Antón

Received: 18 March 2024
Revised: 1 May 2024
Accepted: 6 May 2024
Published: 10 May 2024

1. Introduction

The Earth's climate system is influenced by aerosols from both anthropogenic and natural sources. Aerosols impact the atmospheric radiative balance both directly, through the absorption and scattering of solar radiation, and indirectly, by modifying the microphysical processes associated with cloud formation and precipitation efficiency [1]. Characterized by its distinctive geographical attributes, the Tibetan Plateau (TP) significantly influences atmospheric circulation and climate dynamics within Asia. The collection of long-term, ground-based observation data is challenging to undertake in this remote, high-altitude region, owing to adverse climatic and geographical conditions, as well as challenging logistics.

Among the parameters used to characterize atmospheric aerosols, Aerosol Optical Depth (AOD) and the Ångström Exponent (AE) are two fundamental optical metrics. AOD is an essential parameter that reflects the extinction properties of aerosols, playing a crucial role in estimating aerosol content, assessing atmospheric pollution levels and analyzing the climate effects of aerosols [2]. Optical property measurements, including AOD and AE, are also derived from satellite observations. Common satellite observations for these measurements include the Moderate Resolution Imaging Spectroradiometer (MODIS), Ozone Monitoring Instrument (OMI), Multi-Angle Imaging Spectroradiometer (MISR) and Cloud-Aerosol LiDAR and Infrared Pathfinder Satellite Observations (CALIPSO), offering global atmospheric information [3]. In satellite remote sensing data for aerosol optical properties, factors such as cloud shielding, surface reflectivity differences and varying inversion algorithms of different satellite sensors contribute to uncertainties in the inversion of aerosol optical properties [4]. Due to the thick cloud cover in the southeast of the TP, aerosol observation data from satellite origins are either scarce or have low accuracy validations [5]. The CE318-T offers advantages such as high time resolution and low uncertainty (approximately 0.01–0.02) in continuous measurements [4,6,7]. This device can provide 15-min measurements of aerosol and water vapor column content, serving as valuable data for atmospheric monitoring.

The Large High Altitude Air Shower Observatory (LHAASO) (29.35°N, 100.13°E) is a dual-purpose facility designed for cosmic ray physics and gamma-ray astronomy studies at TeV and PeV energies [8]. The WFCTA, comprising 18 telescopes, is designed to measure primary cosmic rays in the energy range of 10^{13}–10^{17} eV and to extend the energy scales of direct measurements to extremely high energies, featuring various layouts for different observation modes and energy ranges [9]. LHAASO is located in the center of the Hengduan Mountains, as illustrated in Figure 1b, at the junction of the southeastern edge of the TP, the Yunnan–Guizhou Plateau and the Sichuan Basin, as indicated by the solid black rectangle in Figure 1a. The Hengduan Mountains are the easternmost and southernmost monsoonal temperate glacial region in Eurasia and are sensitive to climate change based on studies with glaciers, environments, temperature and precipitation [10]. However, there are limited studies on AOD variation from ground-based measurements, primarily due to the scarcity of readily accessible data collection in the region. Historically, in 1983 and 1984, the aerosol turbidity coefficient was measured at three different elevations on Yunling Baimang Snow Mountain, with peak values observed in March and April. Since December 2009, the Shangri-La atmospheric background station (28.01°N, 99.44°E, 3580.0 m a.s.l.) has been operational, but variations in AOD measured with a sun photometer have not been reported [11]. In 2017, ground measurements were conducted at the Litang station (30.00°N, 100.16°E, 3950.5 m a.s.l.) by the remote sensing network AERONET. Litang, sharing similar topography with LHAASO, utilized a CE-318 sun photometer, indicating peak values in summer. However, Litang's observations spanned only one year, yielding invalid data for the months of April and June [5]. Additionally, the CE-318 at Litang was installed at an urban station, whereas LHAASO is located in a field less impacted by human activities, offering a more accurate representation of atmospheric background aerosol properties in the Hengduan Mountains and the TP [12]. At LHAASO, the extinction coefficients of surface atmospheric aerosols, derived from CALIPSO data and the Longtin model, were reported in our previous work in 2019 [13]. In 2023, we investigated the mean atmospheric boundary layer height, correlating it with atmospheric aerosols [14]. At LHAASO, four laser systems have been operational since October 2020 to monitor atmospheric aerosols on clear nights [15–20]. In this presentation, the optical properties continuously observed with the CE318-T (made in Cimel) from October 2020 to October 2022 and the potential origins of atmospheric aerosols over LHAASO, will be discussed in detail. Section 2 introduces the meteorological characteristics and data of LHAASO station. Section 3 presents results on the optical properties and potential origins of aerosols, and the final section provides a summary.

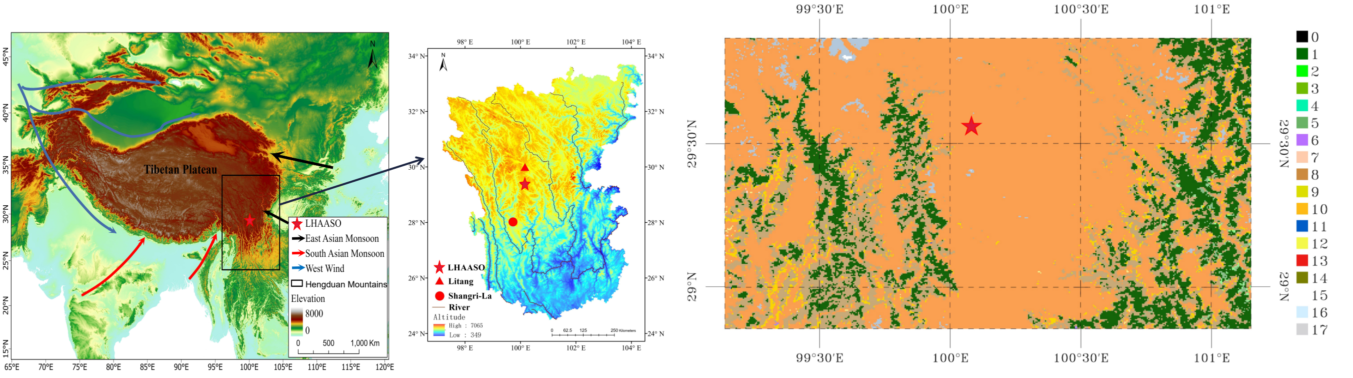

(**a**) (**b**)

Figure 1. (**a**) Large-scale atmospheric circulation and topographic maps (in meters) of TP and the location of the LHAASO. The pentagram means LHAASO site, and the black rectangle around the LHAASO denotes the Hengduan Mountains. Topographic map of Hengduan Mountains [21]. The pentagram means LHAASO site, solid circle represents the Shangri-La station and solid triangle indicates Litang station; brown curves denote the rivers in Hengduan Mountains; different colors means different altitudes (in meters). (**b**) Geomorphological map of LHAASO (adopted from MOD12Q1 products) (0 for water, 1 for evergreen needle leaf, 2 for evergreen broad leaf, 3 for deciduous needle leaf, 4 for deciduous broad leaf, 5 for mixed forests, 6 for closed shrub lands, 7 for open shrub lands, 8 for woody savannahs, 9 for savannahs, 10 for grasslands, 11 for permanent wet lands, 12 for croplands, 13 for urban and built up, 14 for crop nat veg mosaic, 15 for snow and ice, 16 for barren or sparse, 17 for unclassified).

2. Methodology

Observation Site

Both expansive and restrictive definitions exist for the boundary of the Hengduan Mountains. While Liu referred to the expansive definition, we adopt the restrictive definition for this discussion [22]. As depicted in Figure 1a, the Hengduan Mountains (24°40′–34°00′N, 96°20′–104°30′E) are located in the southeastern part of the TP, covering an area of 500,000 km^2 [10]. This region comprises a series of mountain ranges and rivers running from north to south, and the topography declines from northwest to southeast. All the rivers drain into the Pacific Ocean, except for the Nujiang River, which is part of the Indian Ocean water system [21]. Characterized by its north–south rivers and mountains aligned from west to east, it obstructs the East Asia monsoon and serves as a thoroughfare for the South Asia monsoon. The Hengduan Mountains belong to a typical monsoonal climate region, influenced not only by the South Asia monsoon but also by the East Asia monsoon, and affected by the westerlies [10,23].

Topography is a crucial factor influencing AOD. As shown in Figure 1c, LHAASO is characterized by grasslands covered with sandy soil and small rocks, interspersed with a river 1–3 m wide flowing from the southwest to the northeast. Furthermore, LHAASO is relatively isolated from industrial areas and cities, boasting a very limited local population. It is situated in the center of the Haizi Mountain Nature Reserve, spanning from 29.06°N to 30.06°N and from 99.33°E to 100.31°E. Located to the south of Haizi Mountain, the renowned Aden Snow Mountains have an average altitude exceeding 6000 m. The distribution of mountains in the vicinity significantly influences the observation site with local mountain and valley effects.

Compared to satellite observations, ground-based measurements provide more accurate, high-frequency data on aerosol optical properties. Ground-based measurement networks, such as the Aerosol Robotic Network (AERONET), have been deployed worldwide. Ground-based measurements from the CE-318 (CE-318T) sun photometer, widely used in AERONET, are considered the “true value” of measured AOD and are often used to validate satellite-derived AOD products in various regions. The CE318-T offers higher gain and a stronger signal compared to the CE-318. Furthermore, it exhibits a systematic error range between 0.01 and 0.02, indicating a high degree of measurement precision and reliability [7]. As shown in Figure 2a, a CE318-T was installed at LHAASO and has been operational since 26 October 2020. It is calibrated for automatic observations at 15-min intervals. To ensure the representativeness of the observations, we adhered to the uniform aeronautical standard [24]. An observation day was considered valid if there were more than three measurements, the instrument functioned normally and the Sun was not entirely obscured by clouds. To minimize cloud cover impact, we used an infrared cloud-sky instrument that scans the sky in three dimensions, generating a brightness-temperature distribution map of infrared radiation and providing detailed measurements of cloud shape and amount [25]. The criterion for clear days depended on the surface atmospheric temperature and brightness-temperature. As of 25 October 2022, a total of 23,254 datasets from 389 effective observation days have been collected. The monthly measurement statistics are shown in Figure 2b. The data amounts for May, June, July, August, September and October were relatively low, mainly due to the rainy season and the increased number of cloudy days.

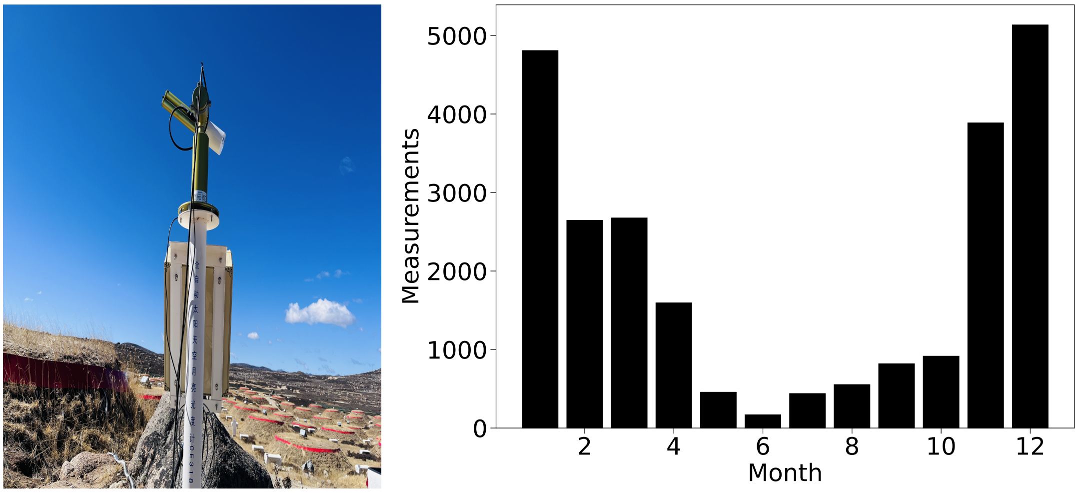

(**a**) (**b**)

Figure 2. (**a**) CE318-T in the field observations. (**b**) The number of measurements vs month; some months may have less data because of the cloudy weather.

3. Results and Discussion

3.1. Meteorological Feature

Meteorological elements significantly influence AOD; however, their contributions vary under different environmental conditions. Temperature often promotes an increase in AOD, while the influence of relative humidity and wind speed on AOD is more complex. On-site measurements of temperature, relative humidity and wind speed are shown in Figure 3. The average temperature for the 2020–2022 measurement period was 1.2 °C, with monthly mean peaking at 9.1 °C and dipping to −9.2 °C. Higher temperatures were recorded from May to October. Similarly, higher relative humidity, exceeding 70%, was observed during the same period. The average annual relative humidity was 60%. In this study, the four common seasons are defined as follows: March to May (spring), June to August (summer), September to November (autumn) and December to February the following year (winter). The average annual wind speed was 2.0 m/s, with monthly mean wind speeds lower in the summer and higher in the other three seasons. Overall, during the winter observation period, conditions were very dry and cold. Meteorological conditions in the near-surface environment undergo seasonal shifts, characterized by fluctuations in air temperature from high to low, relative humidity from wet to dry and near-surface wind intensity from weak to strong. As shown in Figure 4, the southwest wind dominated in all four seasons, correlating well with large-scale atmospheric circulation at 500 hPa at this site, as reported in Xu et al. [26]. Winds blew from more directions in summer, while a similar pattern was observed in the other three season.

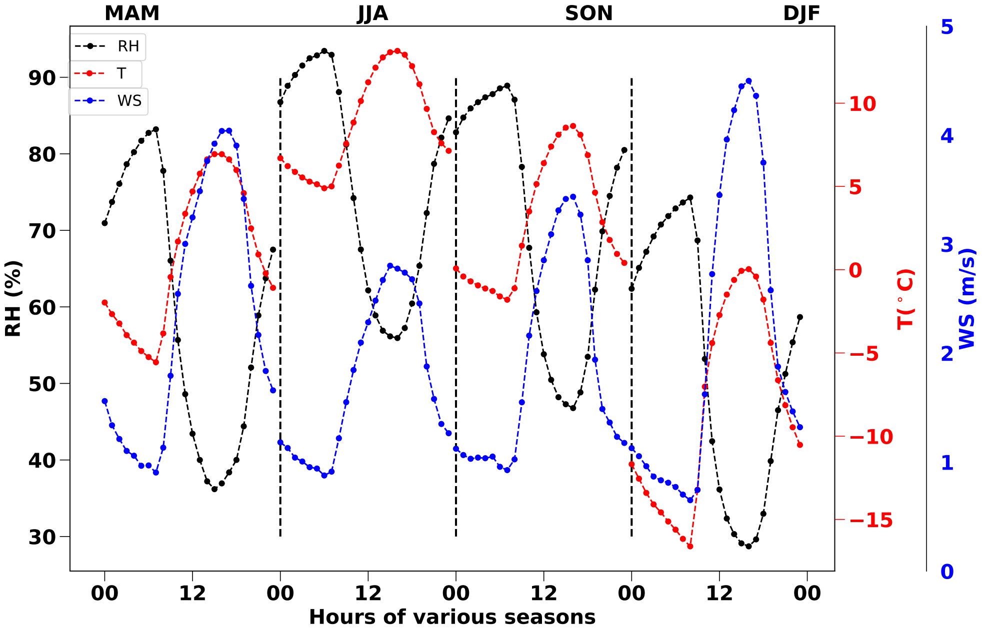

Figure 3. Seasonal diurnal variations in temperature (in red), relative humidity (in black) and wind speed (in blue) during the observation period.

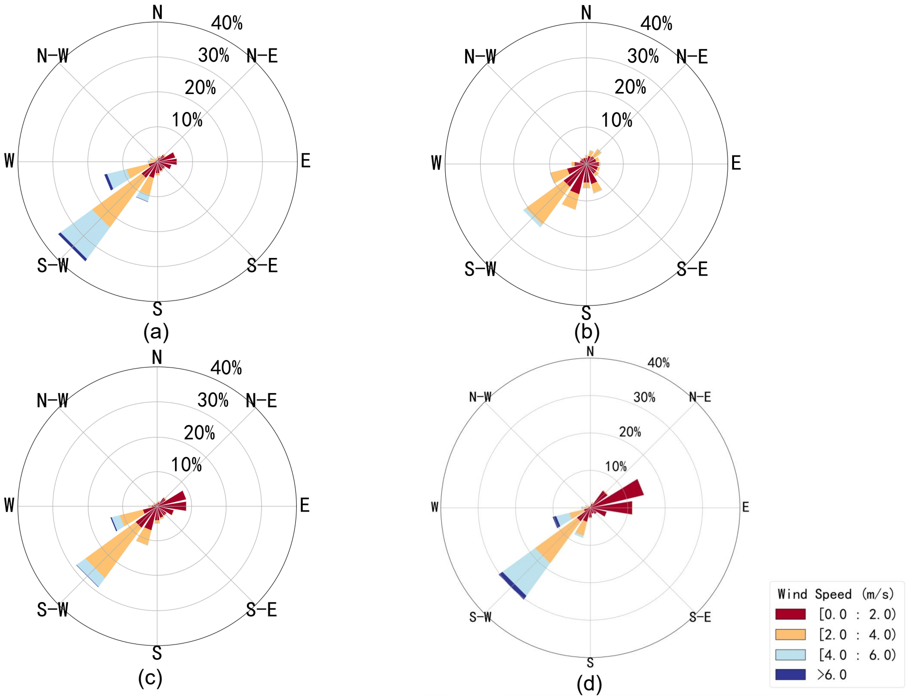

Figure 4. Wind rose plots in different seasons. Hourly horizontal wind direction (WD) was used, with its radii values expressed as percentages for wind blowing from particular directions. (**a**) Spring; (**b**) summer; (**c**) autumn; (**d**) winter.

3.2. Baseline Continental Aerosol at LHAASO

The baseline aerosol refers to the relatively stable and low aerosol loading within an atmosphere unperturbed by human activities. Defined as the median of AOD periods (standard deviation < 0.02 within 4∼5 days), this method was developed for maritime aerosols by Kaufmann et al. [27] and later applied by Xia et al. [28]. Following this method, 63% of the total instantaneous AOD measurements were found stable and used to calculate the baseline value. As shown in Figure 5, the annual baseline AOD and AE were calculated to be 0.030 and 1.075, respectively. The baseline AOD at the NAM-CO and QOMS-CAS stations were 0.029 and 0.027, respectively. Therefore, LHAASO also reflects one of the most pristine regions on Earth, despite being located at the southeastern edge of the TP. The aerosol over LHAASO could serve as a reference state to enhance the assessment of anthropogenic perturbations in the atmosphere [29]. Moreover, this is useful for models estimating aerosol forcing in the current industrial period relative to the preindustrial era in environmental studies [30].

The annual average AOD at 440 nm (AOD_{440nm}) was 0.05 ± 0.03. AE was measured over the 440–870 nm wavelength range, with the annual average $AE_{440–870nm}$ being 1.17 ± 0.30. Table 1 presents a comparison of AOD measurements between LHAASO and other stations on the TP. The annual average AOD_{440nm} at LHAASO was similar to that at the NAM-CO and QOMS-CAS background stations [31], but slightly lower than at Litang and other urban stations [32]. This indicates that LHAASO may have a higher concentration of fine particles compared to NAM-CO and QOMS-CAS background stations, but it is itself still dominated by coarse particles, which may be due to its unique location.

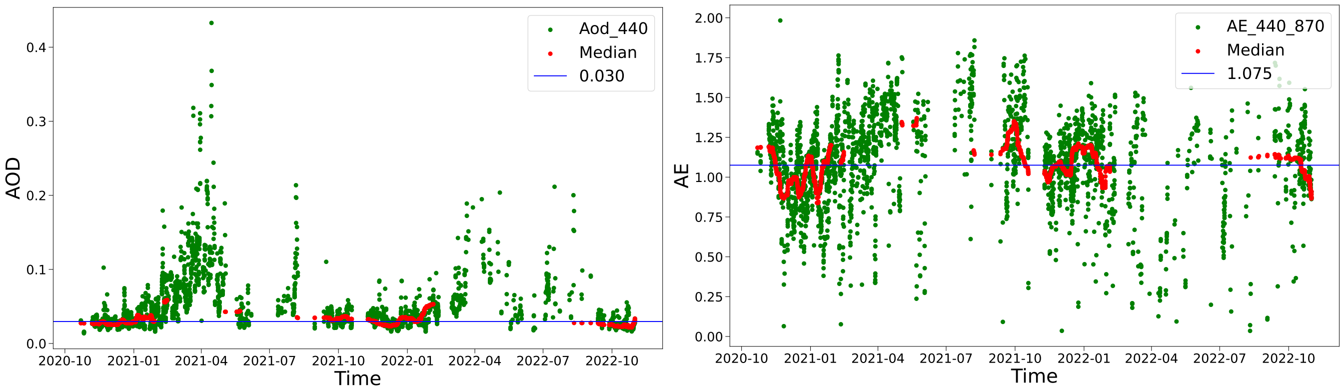

(**a**) (**b**)

Figure 5. (**a**) Time series of AOD. (**b**) Time series of AE. Green symbols represent the instantaneous measurements taken at 15 min intervals. Red symbols are the median of 100 consecutive measurements for standard deviation < 0.02 within 4∼5 days. The blue horizontal line denotes the baseline AOD (AE) value calculated.

Table 1. Annual mean AOD_{440nm} and $AE_{440-870nm}$ in the TP from ground-based sun photometer measurements.

Station	Time Period	AOD_{440nm}	$AE_{440–870nm}$	Site Information
LHAASO	2020.10 –2022.10	0.05 ± 0.03	1.17 ± 0.30	Mountain background station in TP, 29.35°N, 100.13°E, 4410 m a.s.l
Litang	2017.01–2017.12	0.08 ± 0.03	0.72 ± 0.23	Urban station in TP, 30.00°N, 100.16°E, 3950.5 m a.s.l
WLG	2009.09–2012.12	0.14 ± 0.07	0.59 ± 0.24	Background station in TP, 36.28°N, 100.90°E, 3816 m a.s.l
Lhasa	2011.12–2013.12	0.10 ± 0.08	0.67 ± 0.30	Urban station in TP, 29.50°N, 91.13°E, 3648 m a.s.l
NAM−CO	2006.08–2011.01	0.04 ± 0.02	0.94 ± 0.44	Background station in TP, 30.77°N, 90.96°E, 4740 m a.s.l
QOMS−CAS	2010.09–2012.12	0.05 ± 0.29	0.79 ± 0.44	Mountain background station in TP, 28.36°N, 86.95°E, 4276 m a.s.l

3.3. Seasonal Variations of the AOD and AE

To better understand the temporal properties of AOD variation, this study analyzed data spanning the entire period from 2020 to 2022. The mean and median of AOD and AE for each month were calculated, as shown in Figure 6. The aerosol content at LHAASO exhibited a bimodal distribution, with higher values in March, April, July and August. Lower AOD were observed in the remaining months. The monthly mean AOD_{440nm} peaked in April (0.11 ± 0.05) and reached its minimum in December (0.03 ± 0.01). Monthly mean and median AOD from September to January of the following year were close to 0.03, similar to the low at NAM-CO, indicating pristine conditions during these months. These values are comparable to the 0.02 observed at Mauna Loa (3.4 km a.s.l.) in the mid-Pacific [33]. The maximum seasonal mean AOD of 0.08 ± 0.05 is observed during spring, which is notably higher compared to other background sites listed in Table 1, where the spring AE is 1.26 ± 0.25, also higher than typical background levels. This suggests a significant presence of fine, not just coarse, particles in the atmosphere during this season, contrary to the usual expectation of predominantly coarse particles. Such a high AE indicates more efficient scattering by smaller particles, potentially due to regional transport or local seasonal activities contributing to secondary aerosol formation. In summer, although the mean AOD decreases to 0.05 ± 0.03, the AE increases to 1.43 ± 0.27, reaffirming the presence of finer particles possibly augmented by photochemical reactions during warmer months. The AOD in autumn and winter is the lowest, at 0.03 ± 0.01.

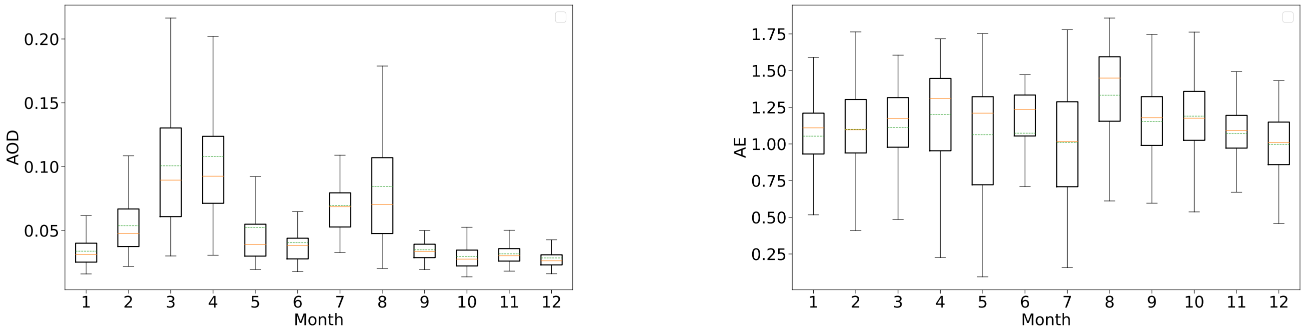

(**a**) (**b**)

Figure 6. (**a**) Box plot of AOD_{440nm}. (**b**) Box plot of $AE_{440–870nm}$. The dotted green line is the mean, the solid orange line is median and the lower and upper bar of the box are first and third quartiles. The lower segment is minimum value, and the upper segment is maximum value.

Overall, the aerosol content at LHAASO was relatively low, indicating a relatively clean atmosphere. Situated in the wilderness at the southeastern edge of the TP, LHAASO is subject to less anthropogenic activity. The overall AOD results indicated higher values in spring and summer, and lower values in autumn and winter. In our findings, the observed increase in AOD and AE during March, April and August not only suggests higher concentrations of particulate matter but specifically indicates the presence of fine and aged particulate matter. This phenomenon likely results from more intensive solar radiation and warmer temperatures accelerating photochemical reactions and secondary aerosol formation during these months. Additionally, the seasonal variation in AOD and AE can be influenced by prevalent atmospheric circulation patterns, which may enhance the long-range transport of fine and aged aerosols from regional biomass burning into the area.

3.4. Diurnal Daytime Variation of AOD and AE

Diurnal variations provide further insights into the underlying factors controlling the evolution of aerosol properties, including emissions, surface heating, reactions, scavenging and wind circulation [34]. The diurnal daytime variations of AOD_{440nm} and $AE_{440–870nm}$ at LHAASO are depicted in Figure 7a,b. It is evident that the diurnal variations of AOD_{440nm}

and $AE_{440–870nm}$ in autumn and winter were generally absent. This finding aligns with expectations for background sites such as QOMS-CAS and NAM-CO station. The most striking diurnal phenomenon occurred in spring at LHAASO, coinciding with the seasonally highest AOD. Specifically, the high AOD in the morning began to decrease at 6:00 local time and remained at a stable low value until 14:00, then further decreased from 15:00 to 19:00 in the evening. This diurnal variation is more pronounced than that at NAM-CO station, which peaks in the morning and then gradually decreases. The decrease in AOD in the afternoon correlated with heavier winds from the southwest. $AE_{440–870nm}$ increased at 7:00 and remained relatively stable until 19:00 in the evening.

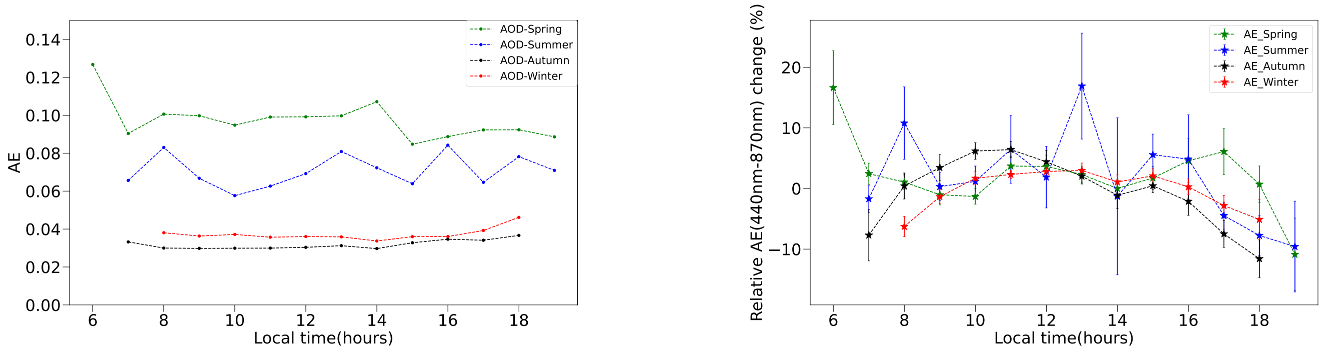

(**a**) (**b**)

Figure 7. Diurnal daytime variation of AOD_{440nm} ($AE_{440–870nm}$) in 4 seasons at LHAASO. The local time is 1.2 h later than Beijing time. (**a**) AOD_{440nm}. (**b**) $AE_{440–870nm}$.

In summer, the AOD variation magnitude of 0.02 was smaller than in spring, with a different diurnal variation trend. $AE_{440–870nm}$ showed a slight increase during the day, from morning to evening, correlated with more rain, lower wind speeds and a higher load of fine particles in the atmosphere. In summer, the alignment of AOD with AE indicates a uniform aerosol type, predominantly fine particles. Conversely, the spring season shows a disconnect, suggesting varied aerosol sources or different atmospheric conditions affecting aerosol properties. This difference between spring and summer may be due to the significant increase in precipitation in summer.

3.5. Characterization of Aerosol Types

The absorbing and scattering capacities of atmospheric aerosols vary according to their types and concentrations. Therefore, classifying aerosol types is crucial for a better understanding of their role in climate and applications in other fields. The 950 nm band information recorded across four seasons by the solar photometer at LHAASO was used to estimate the water vapor content, with an inversion error of about 10%. As shown in Figure 8, AOD_{440nm} did not correlate linearly with water vapor content, as the correlation coefficients were almost zero in all four seasons, indicating that the aerosols over LHAASO did not exhibit significant hygroscopicity [35]. Therefore, the dominant aerosol type at this site comprises non-water-soluble particles, likely including dust and biomass-burning aerosols.

The threshold method for classifying aerosol types based on AOD and AE observations in the TP was developed by Manisha Pokharel [36]. Following this approach, we used AOD at 440 nm wavelength, categorizing $AOD < 0.05$ with $AE < 1.75$ as clean continental background aerosols and $AOD > 0.1$ with $AE > 1.0$ as biomass burning aerosols. Continental background aerosols comprised fine and coarse mode mixtures, with a wide range of AE. Dust events, occasionally appearing over the TP, are characterized by $AOD > 0.1$ and $AE < 0.7$. The remaining cases are considered undetermined or mixed, mainly due to the effects of various aerosol mixing processes occurring in the atmosphere. The boundary lines for different aerosol types are described with red color as shown in Figure 9.

The relationships between AOD and AE, illustrating various aerosol types present in different seasons, are shown in Figure 9. Notably, continental background aerosol was the predominant type in autumn and winter, corresponding well to the pristine conditions over the TP. In spring, several cases of high AOD with fine mode aerosols (i.e., large AE) at LHAASO were identified as biomass burning aerosols from long-range transport. In some extreme events, AOD can increase up to 10 times relative to the baseline values. The higher occurrence of biomass burning aerosols at LHAASO can be attributed to its proximity to South Asia, which more frequently receives agricultural burning and wildfires through long-range transport. In addition, the dust aerosols occurred quite rarely at LHAASO, which may be from the local wind-blown soil particles or transport from the surrounding desert region.

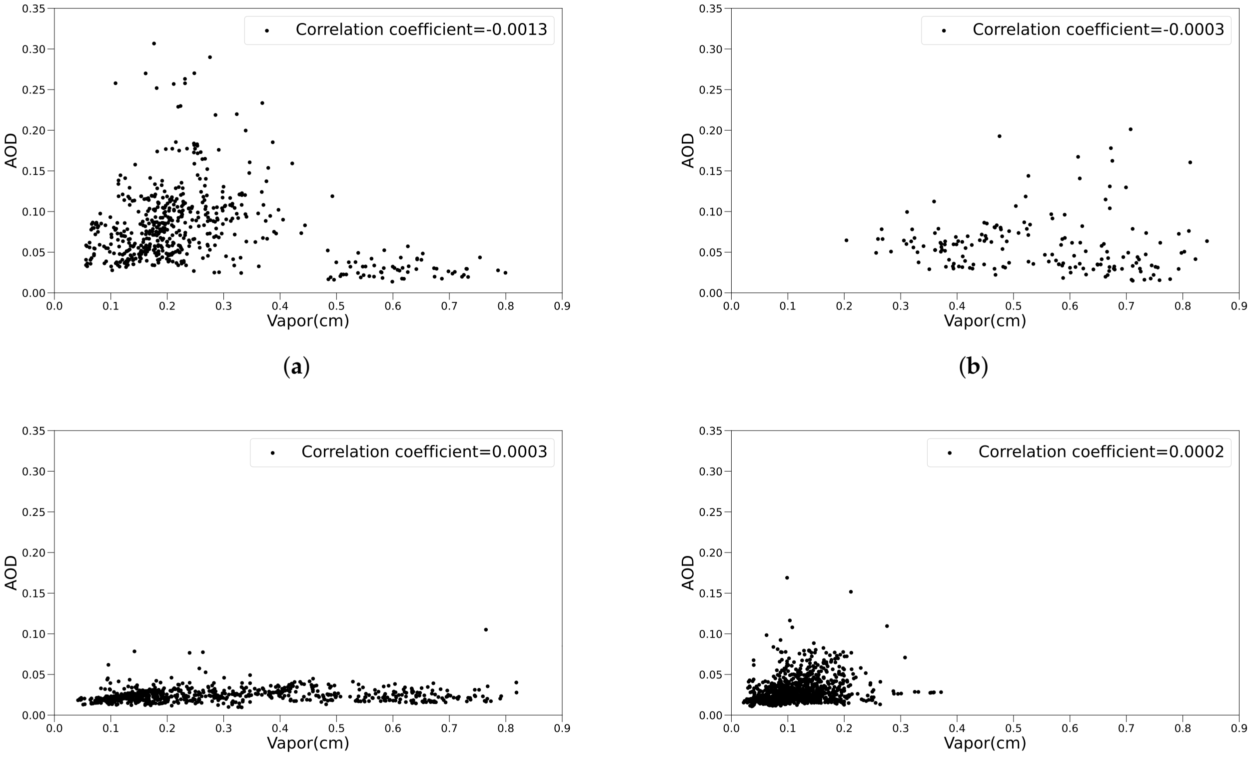

(**a**) (**b**) (**c**) (**d**)

Figure 8. Relationship between AOD_{440nm} and water vapor content during the observation period. (**a**) Spring; (**b**) summer; (**c**) autumn; (**d**) winter.

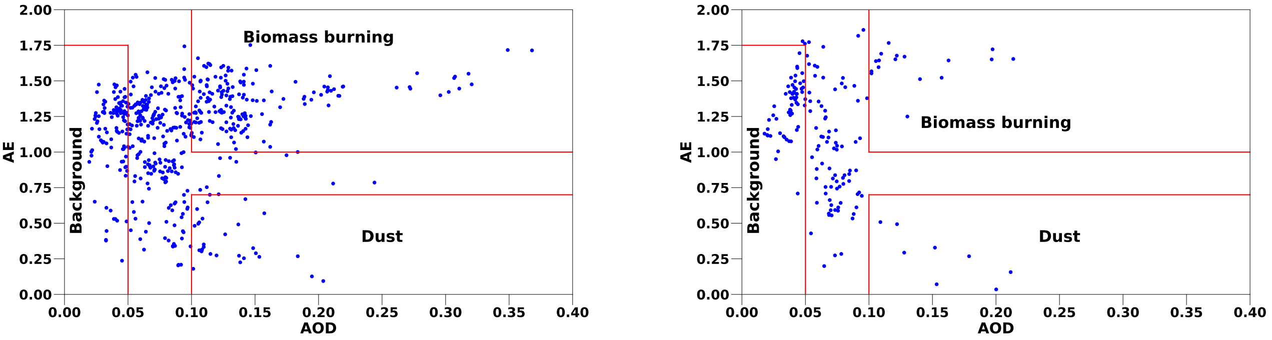

(**a**) (**b**)

Figure 9. *Cont.*

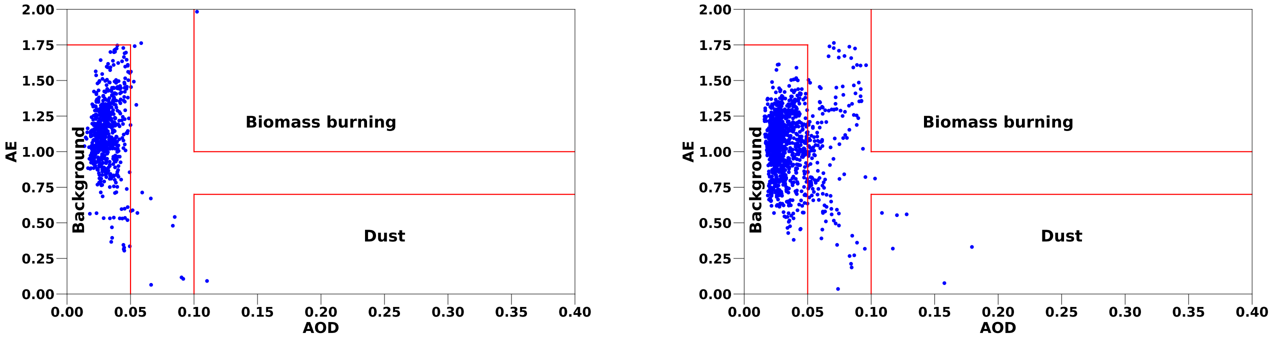

(**c**) (**d**)

Figure 9. Relationship between AOD_{440nm} and $AE_{440–870nm}$ content during the observation period. (**a**) Spring; (**b**) summer; (**c**) autumn; (**d**) winter.

3.6. Analysis of Possible Origins of Aerosols

To identify potential origins of aerosols over the LHAASO region during various periods, the Hybrid Single-Particle Lagrangian Integrated Trajectory model (HYSPLIT) was used to calculate pollutant trajectories. Trajectories with higher aerosol concentrations were selected from a large set to estimate pollutant paths. HYSPLIT uses meteorological field data from the Global Data Assimilation System (GDAS) to calculate 72-h backward trajectories at hourly intervals [37]. The resolution for horizontal and time intervals was set at 1° × 1° and 3 h, respectively. HYSPLIT is widely used in the TP region to trace aerosol origins. For instance, Wang et al. utilized HYSPLIT to study aerosol transport in Nam Co, while Liu et al. applied it to research aerosol transport in Shangri-La [38,39]. MeteoInfo, a suite of software tools for visualizing and analyzing meteorological data, includes the HYSPLIT model [39].

At LHAASO, the mean atmospheric boundary layer height was approximately 900 m in spring, 700 m in summer, 600 m in autumn and 300 m in winter during 2020–2022. Consequently, the starting altitudes for trajectory analyses in the four seasons were set according to these mean heights [14]. Figure 10a depicts the clustering trajectory analysis for spring, predominantly from Northern Myanmar and Northeast India, constituting 86.66% of the total; the remaining origins, located in the southeast of the TP, contribute 13.34%. Figure 10b presents the clustering trajectory analysis for summer, primarily from the China–Myanmar border, accounting for 42.67%; the second largest source is the Sichuan–Yunnan border, contributing 26.05%, followed by the Sichuan Basin at 21.13%, with the remainder in the southwest of the TP accounting for 10.14%. Figure 10c depicts the clustering trajectory analysis for autumn, with the primary source being Northern Myanmar, accounting for 79.52%, followed by the Sichuan–Yunnan border region at 12.89% and the central TP region at 7.59%. Figure 10d presents the clustering trajectory analysis for winter, predominantly from Northern Myanmar, accounting for 75.83%; the second largest source is the northeastern edge of the India border region at 19.05%, with the remainder distributed in the southwest of the TP, accounting for 5.12%.

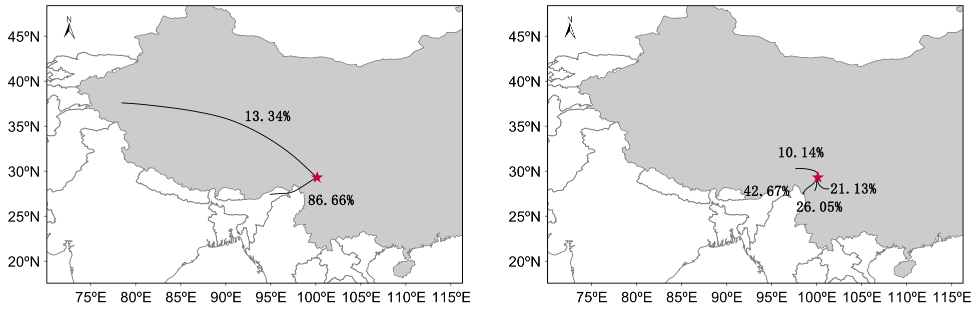

(**a**) (**b**)

Figure 10. *Cont.*

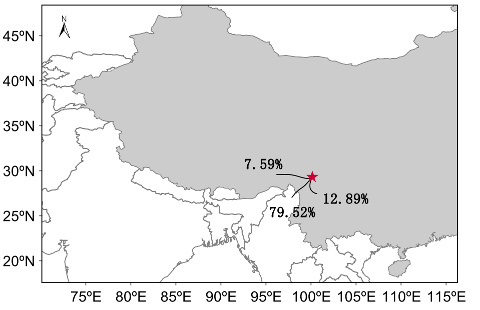

(**c**) (**d**)

Figure 10. The statistics of 72 h backward trajectories from LHAASO in (**a**) spring, (**b**) summer, (**c**) autumn, (**d**) winter. The red pentagram symbol represents the location of LHAASO, and the shaded part represents China. The starting altitudes were fixed at 900 m (spring), 700 m (summer), 600 m (autumn) and 300 m (winter) for the trajectory clustering.

The backward trajectory analyses for the four seasons indicate that over 50% of the air masses arriving at LHAASO originate from the southwest, with a minor proportion coming from the northwest during spring. In summer, air masses also arrive from the northeast and southeast, while in autumn and winter, a few originate from the northwest and northeast.

To analyze the primary sources of high AOD at LHAASO, this study utilized reverse trajectory data from periods of high AOD recorded between 2020 and 2022, applying the following condition: AOD $\geq$ 0.096 [40]. Figure 11a depicts the backward trajectory of screened high AOD, showing that the overall trajectories predominantly originated from the southwest. To more accurately analyze the aerosol source, the backward trajectories were clustered. Figure 11b reveals that the largest aerosol source was from Northern Myanmar and Northeast India, accounting for 80.90%; the secondary main source, indicated to be Central Asia at 14.07%, was primarily transported to LHAASO by the westerly airflow across the TP. The remaining 5.03% originated from the Sichuan–Yunnan border region. This analysis focuses on the largest source of aerosols with the highest AOD.

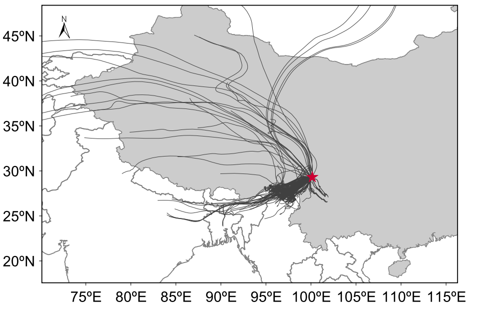

(**a**) (**b**)

Figure 11. AOD $\geq$ 0.096 trajectory screening throughout the year with a starting height of 900 m. The red pentagram symbol represents the location of LHAASO, and the shaded part represents China. (**a**) backward trajectory; (**b**) trajectory clustering.

The issue of aerosol pollution in the southeastern TP is complex, involving various factors, including dust and biomass burning in Southeast Asia. Badarinath et al. indicated significant biomass burning in Northeast India [41]. Shi et al. highlighted that spring is a major period for considerable fire emissions in the northern and northeastern regions of Myanmar [42]. Zhu et al. determined that biomass burning in Myanmar during spring substantially contributes to elevated aerosol concentrations in southeastern China [43]. Fan et al. indicated that air masses arriving at Shangri-La travel through Northeast Myanmar [11].

To investigate the connection between high AOD values and biomass burning, fire occurrence data within the geographical coordinates of 23°N to 29°N and 80°E to 100°E (includes Northern Myanmar and Northeast India) were collected from the MODIS database for the period from October 2020 to October 2022. Analysis of this data, as shown in Figure 12, reveals a significant increase in fire incidents during the spring compared to other times of the year. This seasonal trend aligns with regional observations that indicate heightened activities of biomass burning in the surrounding areas during spring. These findings clearly demonstrate that such activities are key contributors to the elevated aerosol concentrations observed at LHAASO. Importantly, data from the CE318-T dataset show that peak AOD values were recorded in spring, underscoring a robust correlation between increased aerosol levels and the prevalence of forest and agricultural fires. This comprehensive evidence underpins the hypothesis that a significant portion of the aerosols at LHAASO originates from intense springtime burning in Northern Myanmar and Northeast India. Additionally, the analysis of air mass trajectories from 2020 to 2022 at LHAASO indicates that aerosols from these regions are likely transported to the observatory by the southwest bypass of the westerly winds, confirming the role of Northern Myanmar and Northeast India as primary aerosol sources during this season.

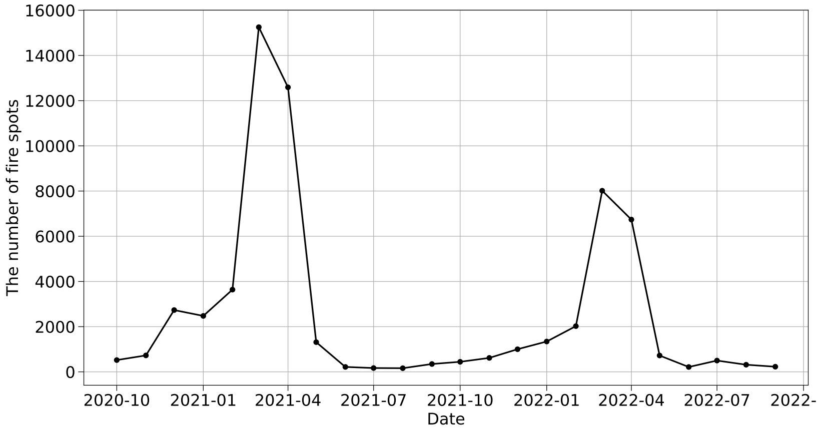

Figure 12. The number of fire spots varied over time.

3.7. Discussion

Our study offers an in-depth examination of aerosol optical properties in the LHAASO region on the eastern edge of the Tibetan Plateau, utilizing a substantial dataset gathered by the CE318-T sun photometer. Our methodology was meticulous, utilizing advanced analytical techniques over an extensive two-year dataset, which underscores the significant strength of our study. LHAASO is situated at a considerably high altitude, offering a distinctive setting that minimizes local pollution influences. This advantageous location facilitates the study of baseline atmospheric conditions and the dynamics of long-range aerosol transport across the Tibetan Plateau.

Despite these strengths, our study faces several limitations. A notable limitation is the lack of direct PM2.5 measurements, which limits our ability to directly correlate observed AOD values with specific concentrations of particulate matter. Additionally, while our dataset effectively outlines seasonal trends, it may not capture the full spectrum of short-term aerosol events or the complete diversity of aerosol types that can be present, due to the intrinsic limitations associated with sun photometry.

To overcome these shortcomings and to build upon our findings, future research should include direct measurements of particulate matter. This enhancement will enable a more accurate correlation between AOD and PM2.5 levels, providing a clearer understanding of aerosol compositions. Incorporating a multi-instrument approach, such as adding lidar systems, would also improve vertical profiling capabilities, thus offering more detailed insights into the stratification and dynamics of aerosols.

Moreover, extending the duration of data monitoring beyond the current two-year period is crucial. Longer-term monitoring would allow for a better understanding of interannual variations and the underlying drivers of aerosol distribution over the Tibetan Plateau, enhancing the predictive accuracy of atmospheric models and contributing to global climate change studies. This extended data collection will be invaluable in confirming seasonal trends and in observing the effects of climatic and environmental policies on regional and global air quality.

4. Summary

TP plays a crucial role in atmospheric circulation, energy budget and hydrological cycles in Asia and globally, influenced by both dynamical and thermal processes. Therefore, investigating the impact of aerosols on the climate and environment over the TP is significantly important. To this end, changes in AOD and AE over time were analyzed using CE318-T data from October 2020 to October 2022.

Data analysis revealed that the annual average $\text{AOD}_{440\text{nm}}$ was 0.05 ± 0.03, and the annual average $\text{AE}_{440\text{–}870\text{nm}}$ was 1.17 ± 0.30. The baseline AOD and AE values were calculated as 0.030 and 1.07, respectively. The monthly average maximum of $\text{AOD}_{440\text{nm}}$ was observed in April (0.11 ± 0.05) and the minimum in December (0.03 ± 0.01). The association between AOD and vapor suggested that the aerosols in the region are predominantly non-water soluble particles. Seasonal characterization of aerosol types revealed that clean continental background aerosol was the predominant type in autumn and winter. In spring and summer, there were instances of biomass burning aerosols transported over long distances from Northern Myanmar, the Northeast India region and the China–Myanmar border. Dust aerosols occurred infrequently at LHAASO throughout the four seasons, likely originating from local wind-blown soil particles or transported from the surrounding desert region.

MeteoInfo software was used to monitor pollution origins and atmospheric trajectories at LHAASO across the four seasons. Subsequently, backward trajectories with elevated AOD values were identified and grouped into distinct clusters. The majority of aerosol particles over LHAASO likely originated from Northern Myanmar and Northeast India. These findings can offer significant evidence and guidance for the precise calibration of photon quantities, the reconstruction of extensive atmospheric showers detected by LHAASO-WFCTA and the assessment of aerosols through the employment of the WFCTA laser system.

Author Contributions: Conceptualization, J.L. and L.X.; methodology, G.Y.; software, Q.S.; validation, X.Z., T.S. and H.L.; formal analysis, M.J.; investigation, L.C.; data curation, Y.W.; writing—original draft preparation, J.X.; writing—review and editing, Y.L.; visualization, F.Z. All authors have read and agreed to the published version of the manuscript.

Funding: This research was funded by the Science and Technology Department of Sichuan Province (grant numbers 2021YFSY0030, 2021YFSY0031).

Data Availability Statement: Dataset available on request from the authors.

Acknowledgments: This work is supported by the Science and Technology Department of Sichuan Province (grant numbers 2021YFSY0030, 2021YFSY0031), and by National Key R&D program of China (grant number 2021YFA0718403). We would like to acknowledge the NOAA Air Reorigins Laboratory team for providing the HYSPLIT−4 trajectory model. The observation data of CE-318T were obtained from the cooperative observation of the Institute of Plateau Meteorology of Chengdu, China Meteorological Administration in LHAASO. We wish to express our gratitude to S.S. Zhang, Y. Zhang, Jiangbazhaxi, H. Q. Zhang, Silangdazhu, Angwangsilang, Ouzhu, Haiweizhang, who helped to operate and maintain the CE-318T.

Conflicts of Interest: The authors declare no conflicts of interest.

References

1. Ramanathan, V.; Crutzen, P.J.; Kiehl, J.; Rosenfeld, D. Aerosols, climate, and the hydrological cycle. *Science* **2001**, *294*, 2119–2124. [CrossRef] [PubMed]
2. Schuster, G.L.; Dubovik, O.; Holben, B.N. Angstrom exponent and bimodal aerosol size distributions. *J. Geophys. Res. Atmos.* **2006**, *111*. [CrossRef]
3. Bibi, H.; Alam, K.; Chishtie, F.; Bibi, S.; Shahid, I.; Blaschke, T. Intercomparison of MODIS, MISR, OMI, and CALIPSO aerosol optical depth retrievals for four locations on the Indo-Gangetic plains and validation against AERONET data. *Atmos. Environ.* **2015**, *111*, 113. [CrossRef]
4. Mehta, M.; Singh, R.; Singh, A.; Singh, N. Recent global Aerosol Optical Depth variations and trends—A comparative study using MODIS and MISR level 3 datasets. *Remote Sens. Environ.* **2016**, *181*, 137. [CrossRef]
5. You, Y.C.; Zhao, T.L.; Xie, Y.; Zheng, Y.; Zhu, J.; Xia, J.; Cao, L.; Wang, C.; Che, H.; Liao, Y.; et al. Variation of the aerosol optical properties and validation of MODIS AOD products over the eastern edge of the Tibetan Plateau based on ground-based remote sensing in 2017. *Atmos. Environ.* **2020**, *223*, 117257. [CrossRef]
6. Wu, L.; Lv, X.; Qin, K.; Bai, Y.; Li, J.; Ren, C.; Zhang, Y. Analysis to Xuzhou aerosol optical characteristics with ground–based measurements by sun photometer. *Chin. Sci. Bull.* **2016**, *61*, 2287.
7. Barreto, Á.; Cuevas, E.; Granados-Muñoz, M.J.; Alados-Arboledas, L.; Romero, P.M.; Gröbner, J.; Kouremeti, N.; Almansa, A.F.; Stone, T.; Toledano, C.; et al. The new sun-sky-lunar Cimel CE318-T multiband photometer–a comprehensive performance evaluation. *Atmos. Meas. Tech.* **2016**, *9*, 631. [CrossRef]
8. Cao, Z.; Aharonian, F.; An, Q.; Axikegu; Bai, L.; Bai, Y.; Bao, Y.; Bastieri, D.; Bi, X.; Bi, Y.; et al. Ultrahigh-energy photons up to 1.4 petaelectronvolts from 12 γ-ray Galactic sources. *Nature* **2021**, *594*, 33. [CrossRef]
9. Cao, Z.; Chen, M.J.; Song-Zhan, C.; Hong-Bo, H.; Cheng, L.; Ye, L.; Ling-Ling, M.; Xin-Hua, M.; Xiang-Dong, S.; Han-Rong, W.; et al. Introduction to Large High Altitude Air Shower Observatory (LHAASO). *Chin. Astron. Astrophys.* **2019**, *43*, 457. [CrossRef]
10. Li, Z.X.; He, Y.Q.; Wang, C.; Wang, X.; Xin, H.; Zhang, W.; Cao, W. Spatial and temporal trends of temperature and precipitation during 1960–2008 at the Hengduan Mountains, China. *Quat. Int.* **2011**, *236*, 127. [CrossRef]
11. Fan, J.S.; Shao, L.Y.; Hu, Y.; Wang, J.; Wang, J.; Ma, J. Classification and chemical compositions of individual particles at an eastern marginal site of Tibetan Plateau. *Atmos. Pollut. Res.* **2016**, *7*, 833. [CrossRef]
12. Liu, B.; Cong, Z.Y.; Wang, Y.; Xin, J.; Wan, X.; Pan, Y.; Liu, Z.; Wang, Y.; Zhang, G.; Wang, Z.; et al. Background aerosol over the Himalayas and Tibetan Plateau: Observed characteristics of aerosol mass loading. *Atmos. Chem. Phys.* **2017**, *17*, 449. [CrossRef]
13. Pi, W.X.; Huang, M.; Zhu, F.R.; He, Y.; Xie, N.; Zhang, Y.; Chen, Q.H.; Jia, H.Y. Extinction coefficients of surface atmospheric aerosol above LHAASO. *Chin. Physics C* **2019**, *43*, 085001. [CrossRef]
14. Liu, J.; Tang, X.F.; Xia, J.J.; Zhu, F.R. Variation of the Atmospheric Boundary Layer Height at the Eastern Edge of the Tibetan Plateau. *arXiv* **2023**, arXiv:2306.01358. [CrossRef]
15. Zhu, F.R.; Zhang, Y.; Xie, N.; Jia, H.Y.; Li, X.M. Study on the calibration optimization of the laser lidar for WFCTA of LHAASO. In Proceedings of the 35th International Cosmic Ray Conference, Busan, Republic of Korea, 12–20 July 2017; Volume 301, p. 366. [CrossRef]
16. Xie, N.; Liu, H.; Hu, Y.; Long, W.; Jia, H.; Zhu, F.; Chen, Q. The Performance of the Laser Systems in the Calibration System of LHAASO-WFCTA. In Proceedings of the 36th International Cosmic Ray Conference (ICRC2019), Madison, WI, USA, 24 July–1 August 2019; Volume 358, p. 498. [CrossRef]
17. Chen, L.; Li, X.; Ge, L.; Liu, H.; Sun, Q.; Wang, Y.; Xia, J.; Zhu, F.; Zhang, Y. Application of the nitrogen laser calibration system in LHAASO-WFCTA. In Proceedings of the 37th International Cosmic Ray Conference, Berlin, Germany, 15–22 July 2021; Volume 395, p. 269. [CrossRef]
18. Sun, Q.N.; Geng, L.S.; Li, X.; Chen, L.; Liu, H.; Wang, Y.; Zhu, F.; Zhang, Y.; Ji, X.; Collaboration, L.; et al. The YAG Lidar System Applied in LHAASO. *In Proceedings of the 37th International Cosmic Ray Conference, Berlin, Germany, 15–22 July 2021* Volume 395, p. 272. [CrossRef]
19. Sun, Q.N.; Zhu, F.R.; Zhang, Y.; Chen, L.; Zhang, S.; Geng, L.; Liu, H.; Min, Z.; Wang, Y.; Wang, Y.; et al. Properties and performance of nitrogen laser systems for calibration of LHAASO-WFCTA. *Nucl. Instrum. Methods Phys. Res. Sect. A Accel. Spectrometers Detect. Assoc. Equip.* **2023**, *1057*, 168759. [CrossRef]
20. Sun, Q.N.; Xie, L.; Yuan, G.; Chen, L.; Wang, Y.; Zhu, F.; Zhang, Y.; Zhang, S. Design and development of laser temperature control system of LHAASO. *J. Instrum.* **2023**, *18*, T06008. [CrossRef]
21. Tao, W.C.; Huang, G.; Dong, D.; Wang, P.; Yu, T.; Gong, H. Dominant modes of interannual variability in precipitation over the Hengduan Mountains during rainy seasons. *Int. J. Climatol.* **2021**, *41*, 2795. [CrossRef]
22. Liu, Y.; Zhao, L. The preliminary analysis of sunshine durations with meteorological data for the Chinese Giant Solar Telescope site survey. *Mon. Not. R. Astron. Soc.* **2013**, *434*, 1674. [CrossRef]
23. Fan, W.W.; Hu, Z.Y.; Xun, X.; Yang, Y.X.; Yu, H.P.; Fu, C.W.; Wu, D. Review of Qinghai-Xizang Plateau monsoon's evolution and climatic effects. *Plateau Meteorol.* **2021**, *40*, 1294.
24. Tanré, D.; Kaufman, Y.; Holben, B.E.A.; Chatenet, B.; Karnieli, A.; Lavenu, F.; Blarel, L.; Dubovik, O.; Remer, L.; Smirnov, A. Climatology of dust aerosol size distribution and optical properties derived from remotely sensed data in the solar spectrum. *J. Geophys. Res. Atmos.* **2001**, *106*, 18205. [CrossRef]

25. Smith, S.; Toumi, R. Measuring cloud cover and brightness temperature with a ground-based thermal infrared camera. *J. Appl. Meteorol. Climatol.* **2008**, *47*, 683. [CrossRef]
26. Xu, C.; Ma, Y.; You, C.; Zhu, Z. The regional distribution characteristics of Aerosol Optical Depth over the Tibetan Plateau. *Atmos. Chem. Phys.* **2015**, *15*, 12065. [CrossRef]
27. Kaufman, Y.J.; Smirnov, A.; Holben, B.N.; Dubovik, O. Baseline maritime aerosol: Methodology to derive the optical thickness and scattering properties. *Geophys. Res. Lett.* **2001**, *28*, 3251. [CrossRef]
28. Xia, X.; Zong, X.; Cong, Z.; Chen, H.; Kang, S.; Wang, P. Baseline continental aerosol over the central Tibetan Plateau and a case study of aerosol transport from South Asia. *Atmos. Environ.* **2011**, *45*, 7370. [CrossRef]
29. Andreae, M.O. Aerosols before pollution. *Science* **2007**, *315*, 50. [CrossRef]
30. Hamilton, D.S.; Lee, L.A.; Pringle, K.J.; Reddington, C.L.; Spracklen, D.V.; Carslaw, K.S. Occurrence of pristine aerosol environments on a polluted planet. *Proc. Natl. Acad. Sci. USA* **2014**, *111*, 18466. [CrossRef]
31. Xia, X.; Che, H.; Zhu, J.; Chen, H.; Cong, Z.; Deng, X.; Fan, X.; Fu, Y.; Goloub, P.; Jiang, H.; et al. Ground-based remote sensing of aerosol climatology in China: Aerosol optical properties, direct radiative effect and its parameterization. *Atmos. Environ.* **2016**, *124*, 243. [CrossRef]
32. Che, H.; Wang, Y.; Sun, J. Aerosol optical properties at Mt. Waliguan Observatory, China. *Atmos. Environ.* **2011**, *45*, 6004. [CrossRef]
33. Holben, B.N.; Tanre, D.; Smirnov, A.; Eck, T.; Slutsker, I.; Abuhassan, N.; Newcomb, W.; Schafer, J.; Chatenet, B.; Lavenu, F.; et al. An emerging ground-based aerosol climatology: Aerosol Optical Depth from AERONET. *J. Geophys. Res. Atmos.* **2001**, *106*, 12067. [CrossRef]
34. Zhang, Y.; Yu, H.; Eck, T.F.; Smirnov, A.; Chin, M.; Remer, L.A.; Bian, H.; Tan, Q.; Levy, R.; Holben, B.N.; et al. Aerosol daytime variations over North and South America derived from multiyear AERONET measurements. *J. Geophys. Res. Atmos.* **2012**, *117*. [CrossRef]
35. Smirnov, A.; Holben, B.N.; Dubovik, O.; O'Neill, N.T.; Eck, T.F.; Westphal, D.L.; Goroch, A.K.; Pietras, C.; Slutsker, I. Atmospheric aerosol optical properties in the Persian Gulf. *J. Atmos. Sci.* **2002**, *59*, 620. [CrossRef]
36. Pokharel, M.; Guang, J.; Liu, B.; Kang, S.; Ma, Y.; Holben, B.N.; Xia, X.; Xin, J.; Ram, K.; Rupakheti, D.; et al. Aerosol properties over Tibetan Plateau from a decade of AERONET measurements: Baseline, types, and influencing factors. *J. Geophys. Res. Atmos.* **2019**, *124*, 13357. [CrossRef]
37. Kleist, D.T.; Parrish, D.F.; Derber, J.C.; Treadon, R.; Wu, W.S.; Lord, S. Introduction of the GSI into the NCEP global data assimilation system. *Weather. Forecast.* **2009**, *24*, 1691. [CrossRef]
38. Wang, J.Y.; Cao, X.J.; Li, M.; Tang, C.; Zhang, Z.; Zhang, H.; Tian, P.; Liang, J.; Zhang, L.; Shi, J. Optical characteristics of aerosol and its potential sources over Nam Co in the Tibetan Plateau during Asian summer monsoon period. *Atmos. Environ.* **2023**, *298*, 119611. [CrossRef]
39. Wang, Y.Q. MeteoInfo: GIS software for meteorological data visualization and analysis. *Meteorol. Appl.* **2014**, *21*, 360. [CrossRef]
40. Aab, A.; Abreu, P.; Aglietta, M.; Ahlers, M.; Ahn, E.; Albuquerque, I.; Allekotte, I.; Allen, J.; Allison, P.; Almela, A.; et al. Origin of atmospheric aerosols at the Pierre Auger Observatory using studies of air mass trajectories in South America. *Atmos. Environ.* **2014**, *149*, 120. [CrossRef]
41. Badarinath, K.; Madhavi Latha, K.; Kiran Chand, T.; Gupta, P.K.; Ghosh, A.; Jain, S.; Gera, B.; Singh, R.; Sarkar, A.; Singh, N.; et al. Characterization of aerosols from biomass burning–A case study from Mizoram (Northeast), India. *Chemosphere* **2004**, *54*, 167. [CrossRef] [PubMed]
42. Shi, Y.S.; Sa Sai, T.; Yamaguchi, Y. Spatio-temporal evaluation of carbon emissions from biomass burning in Southeast Asia during the period 2001–2010. *Ecol. Model.* **2014**, *272*, 98. [CrossRef]
43. Zhu, J.; Xia, X.; Che, H.; Wang, J.; Zhang, J.; Duan, Y. Study of aerosol optical properties at Kunming in southwest China and long-range transport of biomass burning aerosols from North Burma. *Atmos. Res.* **2016**, *169*, 237. [CrossRef]